

Performance of particle swarm optimization on the fully-coherent all-sky search for gravitational waves from compact binary coalescences

Thilina S. Weerathunga

*Department of Physics and Astronomy, University of Texas San Antonio,
One UTSA Circle, San Antonio, Texas 78249, USA*

Soumya D. Mohanty

*Department of Physics and Astronomy, University of Texas Rio Grande Valley,
One West University Boulevard, Brownsville, Texas 78520, USA
(Received 13 April 2017; published 16 June 2017)*

Fully coherent all-sky search for gravitational wave (GW) signals from the coalescence of compact object binaries is a computationally expensive task. Approximations, such as semicoherent coincidence searches, are currently used to circumvent the computational barrier with a concomitant loss in sensitivity. We explore the effectiveness of particle swarm optimization (PSO) in addressing this problem. Our results, using a simulated network of detectors with initial LIGO design sensitivities and a realistic signal strength, show that PSO can successfully deliver a fully coherent all-sky search with $<1/10$ the number of likelihood evaluations needed for a grid-based search.

DOI: 10.1103/PhysRevD.95.124030

I. INTRODUCTION

The detection of gravitational waves, announced in 2016 by the LIGO-Virgo Scientific Collaboration [1], has launched the new era of gravitational wave (GW) astronomy. The detected signals, known as GW150914 [2,3] and GW151226 [4], are best matched by compact binary coalescence (CBC) sources consisting of the inspiral and merger of black holes. The signals were detected by the two aLIGO [5] detectors, which are currently undergoing commissioning to reach their design sensitivity. Over the next few years, aLIGO will be joined by a worldwide network of comparable sensitivity detectors, namely, advanced Virgo [6], KAGRA [7], and LIGO-India [8]. Combining the data from this network of geographically distributed second generation detectors will lead to a better overall sensitivity for CBC signals along with better localization on the sky [9]. Prompt localization will enable the study of such events using multiple messengers of information [10].

Given that theoretically computed waveforms for CBC signals are sufficiently reliable over a broad parameter range [11], it is natural to use the generalized likelihood ratio test (GLRT) and maximum-likelihood estimation (MLE) [12] for the detection and estimation, respectively, of such signals. However, both of these methods involve a computationally expensive nonlinear and nonconvex numerical optimization problem. Applied to the data from a network of detectors, the MLE/GLRT approach—called a fully coherent search—requires the localization of the global maximum of the likelihood over an at least nine-dimensional parameter space [13], where the computation of the likelihood at each point requires correlations between pairs of time series involving $\sim O(10^4)$ (for initial LIGO) to $O(10^6)$ (for aLIGO) samples. A brute force grid-based

search for the global maximum is estimated to require $\sim 4 \times 10^6$ likelihood evaluations over the low component mass range of 1 to $3 M_\odot$ in the case of initial LIGO [14], with the number becoming substantially higher in the case of aLIGO. (The cost of a grid-based search is dominated by the exploration of the low mass range due to longer signal durations [14].)

The computational bottleneck in the fully coherent search for CBC signals has restricted the scope of its applicability so far. The fully coherent search has either been used only for targeted sky locations [15] or has been approximated by semicoherent all-sky searches [16]. Semicoherent searches reduce the computational burden by downselecting the number of data segments to analyze in a fully coherent step. The downselection is based on requirements such as the simultaneous crossing of detection thresholds [17] in at least two single-detector (incoherent) searches and closeness of the estimated signal parameters. As shown in [18], a semicoherent search trades off a significant amount of sensitivity for the reduced computational cost, with the detection volume being $\sim 25\%$ smaller than a fully coherent search.

The estimates of computational cost above pertain to the case of CBC waveforms for systems in which the effect of the spins of the binary components is negligible. Moving on to the full parameter space including spins, a grid-based search simply becomes infeasible due to the exponential dependence of the number of points in a grid on the dimensionality of the signal parameter space. Current efforts at finding alternatives to grid-based search in this context have focused on Markov chain Monte Carlo (MCMC) methods [19] and their variants. In [20], MCMC was applied to the parameter estimation problem

for CBC signals when the spin of one binary component was non-negligible. It was found that a typical MCMC chain needs about $O(5 \times 10^6)$ iterations (likelihood evaluations) in order to converge reliably. This is again too high a computational cost to allow coverage of all data and MCMC methods have been used only as a parameter estimation step following a candidate detection.

Fast methods for producing rapid estimates of sky location of a CBC source have been developed [21–23]. In these methods, the subset of so-called intrinsic signal parameters, which are responsible for the bulk of the cost of a grid search, are simply replaced by the values estimated in the computationally cheaper single-detector searches. Under this approximation, the cost of evaluating the likelihood over the remaining parameters can be reduced significantly. Other studies [24,25] have shown that it is possible to find alternative representations of CBC signals that speed up the computation of the likelihood function.

Particle swarm optimization (PSO) [26] is a global optimization method that has proven to be effective across a wide range of application areas [27], including astronomy, such as CMBR analysis [28] and gravitational lensing [29]. In the context of GW data analysis, PSO was first used in [30] for the single-detector CBC search problem, where it was shown to be effective in locating the global maximum of the likelihood despite its ruggedness. In pulsar-timing-array-based GW detection, PSO was used successfully in optimizing an extremely rugged likelihood function over a 12-dimensional search space [31]. Other successful applications of PSO in GW data analysis are growing at a steady rate [32].

In this paper, we explore the effectiveness of PSO in a fully coherent all-sky CBC search. For the purpose of testing PSO, we take a four-detector network, each having the initial LIGO design noise power spectral density (PSD) [33], and use the 2-PN binary inspiral waveform. We investigate the effectiveness of the GLRT and MLE as found by PSO for detection and parameter estimation, respectively.

The rest of the paper is organized as follows. Section II describes the data and signal models used in the paper. Section III presents the objective function to be optimized in a fully coherent all-sky search. The PSO algorithm is described in Sec. IV. The simulation setup and results are described in Sec. V. Our conclusions are presented in Sec. VI.

II. DATA AND SIGNAL MODELS

In the following, the Fourier transform of a function, $a(t)$, of time is denoted by $\tilde{a}(f)$. The strain time series recorded by the I th GW detector in a network of N detectors is

$$x^I(t) = h^I(t) + n^I(t), \quad (1)$$

where $h^I(t)$ is the detector response to the incident GW and $n^I(t)$ denotes detector noise. We will assume that $n^I(t)$ is a realization of a zero-mean, stationary Gaussian stochastic process,

$$E[n^I(t)] = 0, \quad (2)$$

$$E[\tilde{n}^I(f)(\tilde{n}^I(f'))^*] = \frac{1}{2}S_n(f)\delta(f - f'), \quad (3)$$

with $S_n(f)$ denoting the one-sided noise PSD. It does not carry a detector index in this paper because we assume identical PSD for all the detectors.

We use the Earth-centered Earth-fixed frame (ECEF) [34] to define the geometry of the GW detector network and sources. In terms of the transverse-traceless-gauge polarization waveforms $h_+(t)$ and $h_\times(t)$, the strain response of the I th detector is given by

$$\begin{aligned} h^I(t) = & F_+^I(\alpha, \delta, \psi)h_+(t - \Delta^I) \\ & + F_\times^I(\alpha, \delta, \psi)h_\times(t - \Delta^I). \end{aligned} \quad (4)$$

Here, α and δ are the azimuthal and polar angles, respectively, that define the unit vector pointing to the source,

$$\hat{n} = (\cos \alpha \cos \delta, \sin \alpha \cos \delta, \sin \delta), \quad (5)$$

with the direction of propagation of the GW plane wave being $-\hat{n}$. The polarization angle ψ gives the orientation of the wave frame axes orthogonal to \hat{n} with respect to the fiducial basis,

$$e_x^R = (\sin \alpha, -\cos \alpha, 0), \quad (6)$$

$$e_y^R = (-\cos \alpha \sin \delta, -\sin \alpha \sin \delta, \cos \delta), \quad (7)$$

in the same plane. For CBC sources, the minor and major axes of the ellipse formed by the projection of the orbit of the binary on the sky provide the preferred orientation for the wave frame axes. For generic sources, ψ can be set to zero. Δ^I is the time delay between the arrival of the signal at the ECEF origin and the detector,

$$\Delta^I = \frac{r^I \cdot \hat{n}}{c}, \quad (8)$$

where r^I is the position vector of the detector in the ECEF.

F_+^I and F_\times^I are called the antenna pattern functions and they are given by

$$\begin{pmatrix} F_+^I \\ F_\times^I \end{pmatrix} = \begin{pmatrix} \cos 2\psi \sin 2\psi \\ -\sin 2\psi \cos 2\psi \end{pmatrix} \begin{pmatrix} U_+^I \\ U_\times^I \end{pmatrix}. \quad (9)$$

Here, U_+^I and U_\times^I depend on (α, δ) [35] and are defined by

$$U_+^I = \overset{\leftrightarrow}{\epsilon}_+ : \overset{\leftrightarrow}{d}^I, \quad U_\times^I = \overset{\leftrightarrow}{\epsilon}_\times : \overset{\leftrightarrow}{d}^I, \quad (10)$$

where $\overset{\leftrightarrow}{a}$ denotes a tensor and $:$ denotes the contraction operation on tensors. The polarization basis tensors $\overset{\leftrightarrow}{\epsilon}_{+, \times}$ are given by

$$\overset{\leftrightarrow}{\epsilon}_+ = e_x^R \otimes e_x^R - e_y^R \otimes e_y^R, \quad (11)$$

$$\overset{\leftrightarrow}{\epsilon}_\times = e_x^R \otimes e_y^R + e_y^R \otimes e_x^R, \quad (12)$$

while $\overset{\leftrightarrow}{d}^I$ is the detector tensor

$$\overset{\leftrightarrow}{d}^I = \frac{1}{2} (\hat{u}^I \otimes \hat{u}^I - \hat{v}^I \otimes \hat{v}^I), \quad (13)$$

where (\hat{u}^I, \hat{v}^I) are unit vectors along the arms of the detector. Here, for any given vectors a and b , $(a \otimes b)_{ij} = a_i b_j$.

The relation between the responses of all the detectors in a network, with each appropriately time-shifted to compensate for the delay Δ^I , to the incoming GW strain signal can be expressed in the following compact form,

$$\begin{pmatrix} h^1(t) \\ h^2(t) \\ \vdots \\ h^N(t) \end{pmatrix} = \mathbf{F} \begin{pmatrix} h_+(t) \\ h_\times(t) \end{pmatrix}, \quad (14)$$

where the I^{th} row of \mathbf{F} , called the “antenna pattern matrix,” contains (F_+^I, F_\times^I) . It is known that \mathbf{F} can become rank deficient for certain parts of the sky, leading to an ill-posed inverse problem that can have a significant effect [36–38] on parameter estimation errors. The rank deficiency of \mathbf{F} is quantified in terms of its condition number.

In this paper, we use a four-detector network consisting of the two LIGO detectors at Hanford (H) and Livingston (L), Virgo (V) and Kagra (K). We assume the initial LIGO design PSD [33] for the noise in each detector. The orientations and locations of the detectors, provided in Table I, match their real-world values.

Our choice of the initial LIGO PSD allows data realizations to be considerably shorter in length than what is needed for the PSDs of advanced detectors. This reduces computational costs, which is appropriate for a first investigation of PSO in the context of a fully coherent search.

A. Restricted 2-PN signal

The signal model used in this paper is the restricted 2-PN waveform from a circularized binary consisting of non-spinning compact objects. The phase of the signal is calculated up to order $(v/c)^4$ in the post-Newtonian

TABLE I. Location and orientation vectors for the detectors used in this paper. The vector components are specified in the ECEF. The components (u_x, u_y, u_z) and (v_x, v_y, v_z) are for the unit vectors \hat{u}^I and \hat{v}^I along the detector arms. The components (x, y, z) of the position vector r^I are in meters. The data in this table were obtained from [39,40].

	Hanford	Livingston	Virgo	Kagra
u_x	-0.2239	-0.9546	-0.7005	-0.4300
u_y	0.7998	-0.1416	0.2085	-0.8363
u_z	0.5569	-0.2622	0.6826	0.3400
v_x	-0.9140	0.2977	-0.0538	0.6821
v_y	0.0261	-0.4879	-0.9691	-0.0542
v_z	-0.4049	-0.8205	0.2408	0.7292
x	-2.1614×10^6	-7.4276×10^4	4.5464×10^6	-3.7769×10^6
y	-3.8347×10^6	-5.4963×10^6	8.4299×10^5	3.4839×10^6
z	4.6004×10^6	3.2243×10^6	4.3786×10^6	3.7667×10^6

expansion but the amplitude modulation is calculated only at the lowest (Newtonian) order [41].

The GW polarization waveforms can be expressed conveniently in the Fourier domain using the stationary phase approximation [11],

$$\tilde{h}_+(f) = \frac{\mathcal{A}_f}{r} \frac{(1 + \cos^2 \iota)}{2} f^{-7/6} \exp[-i\Psi(f)], \quad (15)$$

$$\tilde{h}_\times(f) = \frac{\mathcal{A}_f}{r} \cos \iota f^{-7/6} \exp[-i(\Psi(f) + \pi/2)], \quad (16)$$

where r is the distance to the source and the phase $\Psi(f)$ is given by

$$\Psi(f) = 2\pi f t_c - \phi_c - \pi/4 + \sum_{j=0}^4 \alpha_j \left(\frac{f}{f_*} \right)^{(-5+j)/3}. \quad (17)$$

The functional form of α_j is given in the Appendix. They only depend on the component masses m_1 and m_2 through the *chirp times* τ_0 and $\tau_{1.5}$. t_c is the time at which the end of the inspiral signal arrives at the ECEF origin. The amplitude \mathcal{A}_f depends on the component masses m_1 and m_2 . The coalescence phase of the signal is given by ϕ_c . It is possible to absorb r , ϕ_c , ψ , and ι into a new set of parameters A_k , $(k = 1, \dots, 4)$, giving

$$h^I(t) = \sum_{k=1}^4 A_k h_k^I(t), \quad (18)$$

with

$$A_1 = \frac{1}{r} (\beta \cos \phi_c \cos 2\psi - \cos \iota \sin \phi_c \sin 2\psi),$$

$$A_3 = -\frac{1}{r} (\beta \sin \phi_c \cos 2\psi + \cos \iota \cos \phi_c \sin 2\psi), \quad (19)$$

$$\begin{aligned} A_2 &= \frac{1}{r}(\beta \cos \phi_c \sin 2\psi + \cos i \sin \phi_c \cos 2\psi), \\ A_4 &= -\frac{1}{r}(\beta \sin \phi_c \sin 2\psi - \cos i \cos \phi_c \cos 2\psi), \end{aligned} \quad (20)$$

where $\beta = (1 + \cos^2 i)/2$. Here, the waveforms h_k^I , $k = 1, \dots, 4$, are defined as

$$\begin{aligned} h_1^I(t) &= U_+^I h_c(t - \Delta^I), & h_2^I(t) &= U_\times^I h_c(t - \Delta^I), \\ h_3^I(t) &= U_+^I h_s(t - \Delta^I), & h_4^I(t) &= U_\times^I h_s(t - \Delta^I), \end{aligned}$$

with

$$\tilde{h}_c(f) = \mathcal{A}_f f^{-7/6} \exp[-i\Psi(f)|_{\phi_c=0}], \quad (21)$$

$$\tilde{h}_s(f) = -i\tilde{h}_c(f). \quad (22)$$

III. FULLY COHERENT ALL-SKY SEARCH

Under our assumption of Gaussian, stationary noise, the log-likelihood ratio (LLR) [42] for the I th detector is given by

$$\ln \lambda^I = \langle x^I | h^I \rangle - \frac{1}{2} \langle h^I | h^I \rangle, \quad (23)$$

where

$$\langle p | q \rangle = 4\text{Re} \int_0^\infty df \frac{\tilde{p}(f)\tilde{q}^*(f)}{S_n(f)}. \quad (24)$$

If we assume the noise in different detectors to be statistically independent, the log-likelihood for an N detector network is given by

$$\ln \lambda^{(N)} = \sum_{I=1}^N \left[\langle x^I | h^I \rangle - \frac{1}{2} \langle h^I | h^I \rangle \right]. \quad (25)$$

Substituting from Eqs. (18), (19), and (20) we get

$$\ln \lambda^{(N)} = \mathbf{A}^T \mathbf{H} - \frac{1}{2} \mathbf{A}^T \mathbf{M} \mathbf{A}, \quad (26)$$

where $\mathbf{A} = (A_1, A_2, A_3, A_4)^T$, $\mathbf{H} = (H_1, H_2, H_3, H_4)^T$, and $H_a = \sum_{I=1}^N \langle x^I | h_a^I \rangle$ for $a = 1, \dots, 4$. The matrix \mathbf{M} is given by

$$\mathbf{M} = \begin{pmatrix} \mathcal{A} & \mathcal{B} & 0 & 0 \\ \mathcal{B} & \mathcal{C} & 0 & 0 \\ 0 & 0 & \mathcal{A} & \mathcal{B} \\ 0 & 0 & \mathcal{B} & \mathcal{C} \end{pmatrix}, \quad (27)$$

where

$$\begin{aligned} \mathcal{A} &= \sum_{i=1}^N U_+^I U_+^I \langle h_c^I | h_c^I \rangle, \\ \mathcal{B} &= \sum_{i=1}^N U_+^I U_\times^I \langle h_c^I | h_\times^I \rangle, \\ \mathcal{C} &= \sum_{i=1}^N U_\times^I U_\times^I \langle h_c^I | h_c^I \rangle. \end{aligned} \quad (28)$$

It follows that, for a given data realization, the log-likelihood is a function of the parameters \mathbf{A} and $\theta = \{\tau_0, \tau_{1.5}, \alpha, \delta, t_c\}$.

The GLRT statistic is the global maximum of the LLR over the parameters \mathbf{A} and θ . Following [16], it is denoted by the equivalent statistic ρ_{coh} ,

$$\rho_{\text{coh}}^2 = 2 \max_{\mathbf{A}, \theta} \ln \lambda^{(N)}, \quad (29)$$

called the “coherent search statistic.” The MLE, $\hat{\mathbf{A}}$ and $\hat{\theta}$, of \mathbf{A} and θ , respectively, are the maximizers.

The maximization of the log-likelihood can be carried out as

$$\rho_{\text{coh}}^2 = \max_{\theta} \gamma^2(\theta), \quad (30)$$

$$\gamma^2(\theta) = 2 \max_{\mathbf{A}} \ln \lambda^{(N)}. \quad (31)$$

The inner maximization over \mathbf{A} can be performed analytically, giving

$$\hat{\mathbf{A}} = \mathbf{M}^{-1} \mathbf{H} \quad (32)$$

as the solution. Then,

$$\gamma^2(\theta) = \mathbf{H}^T \mathbf{M}^{-1} \mathbf{H}. \quad (33)$$

The outer maximization over θ must be carried out numerically. For fixed $\{\tau_0, \tau_{1.5}, \alpha, \delta\}$, the maximization over t_c can be carried out very efficiently using the fast Fourier transform (FFT) since $\langle p | q(t - t_c) \rangle$ is a correlation operation [16]. We call

$$\Gamma^2(\Theta) = \max_{t_c} \gamma^2(\theta) \Rightarrow \rho_{\text{coh}}^2 = \max_{\Theta} \Gamma^2(\Theta), \quad (34)$$

with $\Theta = \{\tau_0, \tau_{1.5}, \alpha, \delta\}$, the “coherent fitness function.” Its maximization over Θ is the main challenge in the implementation of a fully coherent search. In this paper, we use PSO, described next, to carry out this task.

IV. PARTICLE SWARM OPTIMIZATION

PSO is an optimization method derived from a simplified mathematical model of the swarming behavior observed in nature across many species. It uses a fixed number of

samples (called “particles”) of the function to be optimized (called the “fitness function”). The particles are iteratively moved in the search space following a set of dynamical equations.

A. PSO algorithm

To provide a rigorous description of PSO, we adopt the following notation in this section.

- (i) $f(x)$: The scalar fitness function to be optimized, with $x = (x^1, x^2, \dots, x^d) \in \mathbb{R}^d$. In our case, $x = \Theta$, $f(x)$ is the coherent fitness function $\Gamma^2(\Theta)$ [cf., Eq. (34)] and $d = 4$.
- (ii) $\mathcal{S} \subset \mathbb{R}^d$: The search space defined by the hypercube $a^i \leq x^i \leq b^i$, $i = 1, 2, \dots, d$.
- (iii) N_p : The number of particles in the swarm.
- (iv) $x_i[k]$: The position of the i th particle at the k th iteration.
- (v) $p_i[k]$: The best location found by the i th particle over all iterations up to and including the k th,

$$f(p_i[k]) = \max_{j \leq k} f(x_i[j]). \quad (35)$$

- (vi) $p_g[k]$: The best location found by the swarm over all iterations up to and including the k th,

$$f(p_g[k]) = \max_{1 \leq j \leq N_p} f(x_j[k]). \quad (36)$$

The PSO dynamical equations are as follows:

$$\begin{aligned} v_i[k+1] &= w[k]v_i[k] + c_1\mathbf{r}_1(p_i[k] - x_i[k]) \\ &\quad + c_2\mathbf{r}_2(p_g[k] - x_i[k]). \end{aligned} \quad (37)$$

$$x_i[k+1] = x_i[k] + z_i[k+1], \quad (38)$$

$$z_i^j[k] = \begin{cases} v_i^j[k], & -v_{\max}^j \leq v_i^j[k] \leq v_{\max}^j \\ -v_{\max}^j, & v_i^j[k] < -v_{\max}^j \\ v_{\max}^j & v_i^j[k] > v_{\max}^j \end{cases}. \quad (39)$$

Here, $v_i[k]$ is called the “velocity” of the i th particle; $w[k]$ is a deterministic function known as the inertia weight (see below); c_1 and c_2 are constants; and \mathbf{r}_i is a diagonal matrix with independent, identically distributed random variables having a uniform distribution over $[0, 1]$. The second and third terms on the rhs of Eq. (37) are called the “cognitive” and “social” terms, respectively.

The iterations are initialized at $k = 1$ by independently drawing (i) $x_i^j[1]$ from a uniform distribution over $[a^j, b^j]$, and (ii) $v_i^j[1]$ from a uniform distribution over $[-v_{\max}^j, v_{\max}^j]$.

The behavior of particles must be prescribed when they exit the search space. We adopt the standard “let them fly” boundary condition under which a particle outside the search space is assigned a fitness values of $-\infty$. Since both

$p_i[k]$ and $p_g[k]$ are always within the search space, such a particle is eventually dragged back into the search space by the cognitive and social terms. The stopping criterion adopted is simply that a fixed number, N_{iter} , of iterations are completed.

B. Assessing convergence

The conditions for a stochastic optimizer to converge to the global optimum [43] require that (a) every measurable subset of the search space be visited at least once, and (ii) the fitness value at any iteration be equal to or better than the value at the previous one. There are no stochastic optimization methods, including PSO, that pass these conditions in a finite number of iterations. Hence, convergence to the global maximum is not guaranteed. Note that this does not mean that PSO cannot converge to the global maximum. It simply means that we can never be sure if it has found the global maximum or not. One can only talk about the probability of convergence in a given run of PSO. A simple way to increase this probability to near certainty is to do a sufficient number of independent runs of PSO. If the probability of convergence in a single run is P_{conv} , then the probability of not converging in any of N_{runs} independent runs is $(1 - P_{\text{conv}})^{N_{\text{runs}}}$.

Another issue with using a stochastic optimization method like PSO is that it is not directly possible to verify that the end result of PSO is actually close to the global maximum or not. This is because verification can only be done using a grid search and, for the problem of interest, a grid search may simply be infeasible. (Theoretical studies of PSO use benchmark fitness functions for which the location of the global optimum is known by construction.) However, as pointed out in [30], there exists an indirect way to check if PSO is performing satisfactorily in the case of likelihood maximization with data containing a signal injected with known parameters. Since any parameter estimation method incurs an estimation error caused by the shift of the global maximum away from the true signal parameters, the global maximum of the fitness must be higher than the fitness value at the true signal parameters, the latter being known for simulated data. Thus, we can find out if PSO is doing a satisfactory job or not by checking that it yields a fitness value greater than the one at the true signal parameters.

C. PSO tuning

Stochastic optimizers such as PSO need to trade off wide-ranging *exploration* of the search space against *exploitation* of a good candidate location. These two phases are in conflict with each other, requiring a proper balance in the relative time spent in each phase. In general, more exploration leads to higher computational cost, while making it too short leads to premature convergence to a local maximum. Figure 1 shows the global best-fitness

value evolution for the coherent network analysis problem. One can see how PSO initially converges rapidly during the exploration phase and then slows down while it searches for the best value in a small region during the exploitation phase.

In the version of PSO described here, the main parameter controlling the transition from exploration to exploitation is the inertia weight. In this paper, the inertia weight is chosen to decay linearly from a value w_{\max} at $k = 1$ to w_{\min} at $k = N_{\text{iter}}$.

An attractive feature of PSO is the apparent robustness of its parameter values across a wide range of optimization problems [44]. This greatly reduces the effort needed to tune the algorithm for satisfactory performance. We find that, in the optimization problem considered here, fairly standard settings [45] for the PSO parameters work well. The values used for these parameters are $N_p = 40$, $c_1 = c_2 = 2.0$, $v_{\max}^i = 0.5(b^i - a^i)$, $w_{\max} = 0.9$, and $w_{\min} = 0.3$.

The only parameter above that required any kind of tuning was N_{iter} . To perform the tuning, we examined the evolution of the global best fitness $f(p_g[k])$ as a function of k . The tuning process starts by picking an N_{iter} value that is sufficiently deep in the exploitation phase based on a curve such as Fig. 1. We then do 12 independent runs of PSO with this value of N_{iter} and find the fraction of runs in which the final global best fitness exceeds the fitness at the true signal parameters. This gives an estimate of P_{conv} , the probability of successful convergence. We increase N_{iter} until $P_{\text{conv}} \simeq 0.3$, which gives a probability of failure in 12 independent PSO runs of 0.0138. However, since P_{conv} is estimated using only 12 trials, it is not very accurate. The actual probability of successful convergence is discussed in Sec. V. Based on this tuning procedure, we set $N_{\text{iter}} = 500$.

It is important to note that the PSO algorithm presented here is considered to be one of the most basic among the general class of algorithms that have been proposed under the PSO metaheuristic [46]. An important variant, for

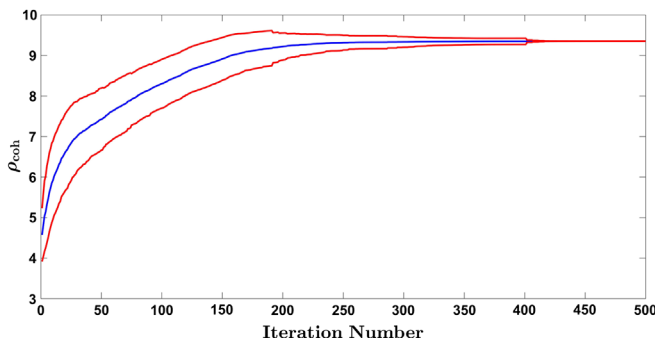


FIG. 1. Evolution of the mean and standard deviation of the coherent search statistic for a single data realization. The blue line is the average over 225 independent PSO runs, while the red curves show the 1σ standard deviation. The data realization contains a signal with a coherent network SNR [defined in Eq. (40)] of 9.0.

example, is the use of a neighborhood best location [47] instead of the global best $p_g[k]$. Another variant [27] applies a constriction factor to the equation for $v_i[k]$ instead of clamping its components to the interval $[-v_{\max}, v_{\max}]$. We did not find it necessary to explore these other variants because the basic version of PSO appears to do a satisfactory job.

V. RESULTS

We test the performance of PSO using simulated realizations of data for the HLVK network described in Sec. II. For each data realization, $N_{\text{runs}} = 12$ independent PSO runs are carried out. The result for each data realization corresponds to the output from the run that achieves the best final value of the coherent search statistic ρ_{coh} . The independent PSO runs are executed in parallel, and the choice of $N_{\text{runs}} = 12$ arises from the 12 processing cores per node in the computing cluster that was used for the analysis.

The simulated signals are normalized to have a specified *coherent network SNR* (SNR_{coh}), defined as

$$\text{SNR}_{\text{coh}} = \gamma(\theta_{\text{true}}) = [H^T M^{-1} H|_{\hat{\mathbf{A}}, \theta_{\text{true}}}]^{1/2}, \quad (40)$$

where θ_{true} denotes the values of $\{\tau_0, \tau_{1.5}, \alpha, \delta, t_c\}$ associated with the signal to be normalized. SNR_{coh} is related to the optimal network signal to noise ratio (SNR_{opt}) by $\text{SNR}_{\text{opt}} \simeq \sqrt{2}\text{SNR}_{\text{coh}}$, where SNR_{opt} is defined as

$$\text{SNR}_{\text{opt}} = \frac{E[\ln \lambda^{(N)} | H_1] - E[\ln \lambda^{(N)} | H_0]}{[E[(\ln \lambda^{(N)} - E[\ln \lambda^{(N)} | H_0])^2 | H_0]]^{1/2}} \quad (41)$$

$$= \left[\sum_{I=1}^N \langle h^I | h^I \rangle \right]^{1/2}. \quad (42)$$

Here, $E[X|A]$ denotes the conditional expectation of a random variable X given condition A . H_0 and H_1 correspond to the cases where a signal is, respectively, absent or present in the data. Normalization using SNR_{opt} assumes the best-case scenario where all the signal parameters, including \mathbf{A} , are known *a priori*, while normalization with SNR_{coh} relaxes this unrealistic assumption somewhat.

We pick several combinations of binary component masses and source sky locations to generate data realizations containing signals. We label these combinations using the scheme MaLb , where $a \in \{1, 2\}$ and $b \in \{1, 2, 3, 4, 5, 6\}$. M1 and M2 refer to the pair of binary component masses $(1.4 M_{\odot}, 1.4 M_{\odot})$ and $(4.6 M_{\odot}, 1.4 M_{\odot})$, respectively. Lb refers to the source sky location, for which the values used are listed in Table II.

For each set, MaLb , of parameters, 120 data realizations are generated. In all cases, the signals are normalized to have $\text{SNR}_{\text{coh}} = 9.0$ (equivalent to $\text{SNR}_{\text{opt}} = 12.7$). In all cases, the signals correspond to face-on binaries with $i = 0$.

TABLE II. Source sky locations used in the simulations. The first column lists the label assigned to the location. The second and third columns list the azimuthal and polar angles of the source location in the ECEF. The condition number of the antenna pattern matrix at each chosen source location is listed in the last column.

Label	α (degrees)	δ (degrees)	\log_{10} (condition number)
L1	80.79	-29.22	0.9711
L2	-128.34	-33.80	0.6079
L3	-81.93	13.75	0.6008
L4	32.09	-53.86	3.2436
L5	150.11	-60.16	0.0066
L6	-122.61	41.25	1.6159

As such, ψ gets absorbed into the coalescence phase parameter, which is set to $\phi_c = \pi/3$ radians.

The degree of ill-posedness in the inverse problem of coherent network analysis can be measured in terms of the condition number [36–38] of the antenna pattern matrix \mathbf{F} . Since the antenna pattern functions depend on the sky location of a source, so does the condition number. The sky locations chosen in Table II sample the condition number across a range of values, corresponding to a well-conditioned (low) to poorly conditioned (high) inverse problem.

For each realization, the data are generated directly in the Fourier domain with a frequency spacing of 0.0156 Hz between consecutive bins and a maximum (Nyquist) frequency of 1024 Hz. In the time domain, this corresponds to a data segment duration of 64 sec sampled at 2048 Hz.

The chirp times corresponding to the two sets of masses used in the simulation are $(\tau_0, \tau_{1.5}) = (24.850, 0.866)$ sec and $(9.751, 0.728)$ sec, respectively. It is assumed that the signals are not visible at frequencies below 40 Hz due to the steep rise in seismic noise below this frequency. Hence, the signal waveform samples are set to zero below this frequency. Similarly, any inspiral signal terminates when the binary components reach the last stable circular orbit. We use 700 Hz, the frequency corresponding to the lower total mass system, as the cutoff frequency for all signal waveforms. The last stable orbit frequency decreases for higher mass systems but, given the small number of cycles at high frequencies, it makes no practical difference to the results if a uniform cutoff frequency is used.

For PSO, we use a search range of (i) $[0, 43.538]$ sec for τ_0 ; (ii) $[0, 1.084]$ sec for $\tau_{1.5}$; (iii) $[-180, 180]$ degrees for right ascension (α); and (iv) $[-90, 90]$ degrees for declination (δ).

A. Detection performance

It is important to note that the value of the coherent search statistic, ρ_{coh} , found by PSO need not be the actual value, namely, the true global maximum of the log-likelihood ratio. Hence, it is important to verify that ρ_{coh} as found by PSO performs well in terms of detection.

Figure 2 shows the distribution of ρ_{coh} found by PSO for data realizations corresponding to (i) the null hypothesis (H_0) with signal absent, and (ii) the alternative hypothesis (H_1) with signal present. For the latter, we have combined the ρ_{coh} values for the 12 source parameter values, MaLb,

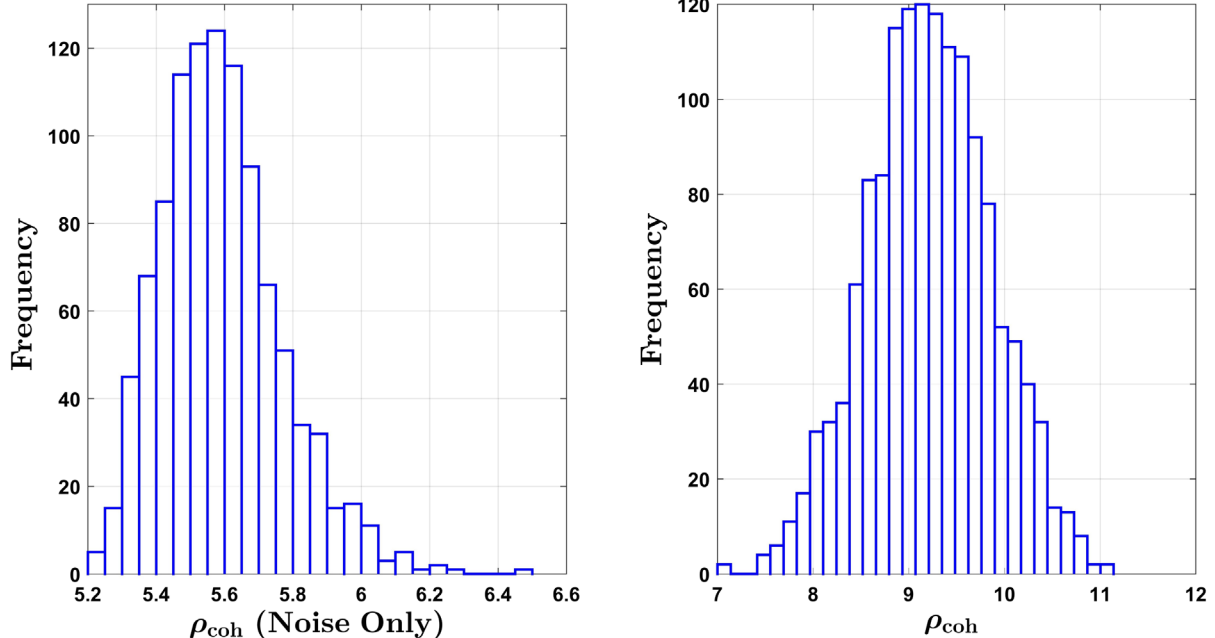


FIG. 2. Distribution of coherent search statistic, ρ_{coh} , values found by PSO. Left: Noise-only case obtained from 1024 independent data realizations. Right: Signal plus noise for $\text{SNR}_{\text{coh}} = 9$. For the latter, we have pooled together the values of ρ_{coh} for all 12 source parameter value sets used in the simulations. This leads to 1440 independent trial values of ρ_{coh} for the histogram on the right.

used in the generation of data realizations containing signals. For the number of data realizations used in our simulations, there is no overlap between the distribution of ρ_{coh} for H_0 and H_1 . This suggests that ρ_{coh} found by PSO performs quite well as a detection statistic and that it is an acceptable surrogate for the true coherent search statistic.

Figure 3 shows a scatterplot of ρ_{coh} found by PSO against the coherent fitness function at the true signal location, $\Gamma(\Theta_{\text{true}})$, where Θ_{true} denotes the known parameters of the signal injected into the data realization. As discussed in Sec. IV B, $\rho_{\text{coh}} \geq \Gamma(\Theta_{\text{true}})$ indicates that PSO has likely found the global maximum. We find that this condition is satisfied in 93.4% of the total number of data realizations when the number of independent PSO runs is set to $N_{\text{runs}} = 12$. Quantifying the departure from this condition in terms of $q = (1 - \rho_{\text{coh}}/\Gamma(\Theta_{\text{true}})) \times 100$, we find that 97.0%, 98.4%, and 99.7% of all trials satisfy $q \leq 3\%$, $\leq 5\%$, and $\leq 10\%$ respectively. When the number of PSO runs is set to $N_{\text{runs}} = 24$ for the realizations that showed a departure from the above condition, the vast majority ended up satisfying the condition again, leading to 99.7%, 99.9%, and 100% of all trials for $q \leq 3\%$, $\leq 5\%$, and $\leq 10\%$, respectively.

While a violation of the condition $\rho_{\text{coh}} \geq \Gamma(\Theta_{\text{true}})$ means a failure to locate the global maximum, the drop in ρ_{coh}

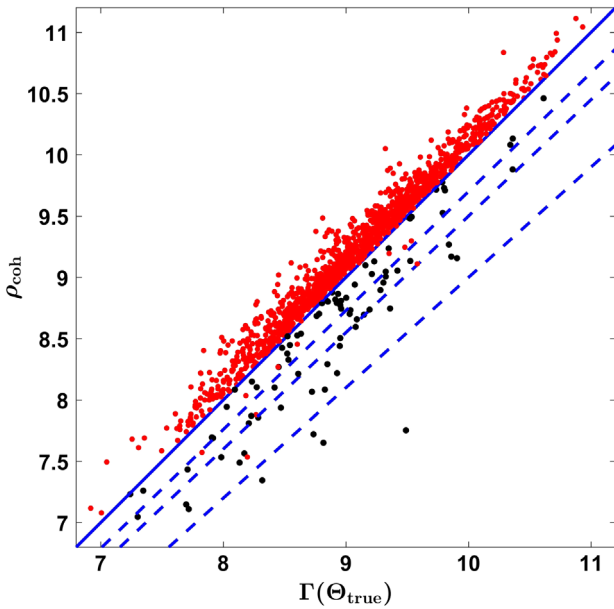


FIG. 3. Comparison of the coherent search statistic ρ_{coh} found by PSO with the coherent fitness value $\Gamma(\Theta_{\text{true}})$ at the true signal parameters, Θ_{true} . Each dot corresponds to one data realization, from a total of 1440 realizations across all the source parameters used. Dashed lines show the 3%, 5%, and 10% drop from the coherent fitness value. Black dots indicate data realizations for which $\rho_{\text{coh}} < \Gamma(\Theta_{\text{true}})$ with $N_{\text{runs}} = 12$ independent PSO runs, but recovered to $\rho_{\text{coh}} \geq \Gamma(\Theta_{\text{true}})$ when $N_{\text{runs}} = 24$. The total number of points below the diagonal is 95.

found by PSO from its true value may be small enough that the detection threshold is still crossed. This would result in the detection of a signal, although it may not provide a good estimate of its parameters. The loss in detection probability can be estimated in terms of the fraction of realizations in which ρ_{coh} found by PSO fell below a given detection threshold while $\Gamma(\Theta_{\text{true}})$ stayed above it. Since the true ρ_{coh} is always greater than $\Gamma(\Theta_{\text{true}})$, the latter condition implies that a detection would have resulted if the true ρ_{coh} were available. For a detection threshold η , we find that the fractional loss in detection probability, given by the number of realizations where $\rho_{\text{coh}} \leq \eta$ and $\Gamma(\Theta_{\text{true}}) \geq \eta$ relative to the number where $\Gamma(\Theta_{\text{true}}) \geq \eta$, is between $\approx 0.9\%$ to $\approx 2.5\%$ for $8.0 \leq \eta \leq 9.0$.

B. Estimation performance

The performance of PSO in estimating the sky location of a source is shown in Fig. 4, with zoomed-in views shown in Figs. 5 and 6. It is evident from Fig. 4 that the distribution of the sky localization error is strongly influenced by the condition number of the antenna pattern matrix [cf. Eq. (14)] at the true location. A source location with a low condition number tends to have a small positional error.

We use the area $16\sigma_\alpha\sigma_\delta \cos\delta$ of the box of side length $4\sigma_\alpha$ and $4\sigma_\delta$, where σ_α and σ_δ are the standard deviations in estimates of α and δ , respectively, as a simple measure of position error. For the sources M1L5 and M2L5 that have the lowest condition number, the position errors are 10.43 and 7.32 deg², respectively. For the highest condition number location (L4), we get 152.45 and 140.39 deg² for M1 and M2, respectively. The highest position error occurs not at the highest condition number but at L6, which is the second highest. However, our simple measure of position error is wholly inapplicable to these extreme locations because the error is distributed along a stretched-out region. A proper estimation of errors for extreme condition numbers requires a much larger number of data realizations in order to map out the error region with a sufficient density of sample points. This is postponed to future work pending ongoing work on increasing the computational efficiency of our codes.

Table III summarizes the marginal distribution of errors up to the second moment for all the signal parameters constituting the PSO search space. No clear trend emerges for the dependence on condition number of the errors in the chirp time parameters τ_0 and $\tau_{1.5}$. It is likely that resolving a dependence, if any, requires a significantly larger number of data realizations. For completeness, the marginal distributions are shown in Figs. 7 and 8. Table IV lists the sample correlation coefficients between pairs of parameters. The sample correlation coefficient between τ_0 and $\tau_{1.5}$ is ≥ 0.9 for all the sources considered here. The strong correlation between chirp time estimates is well known from studies of single-detector searches [49]. It is generally

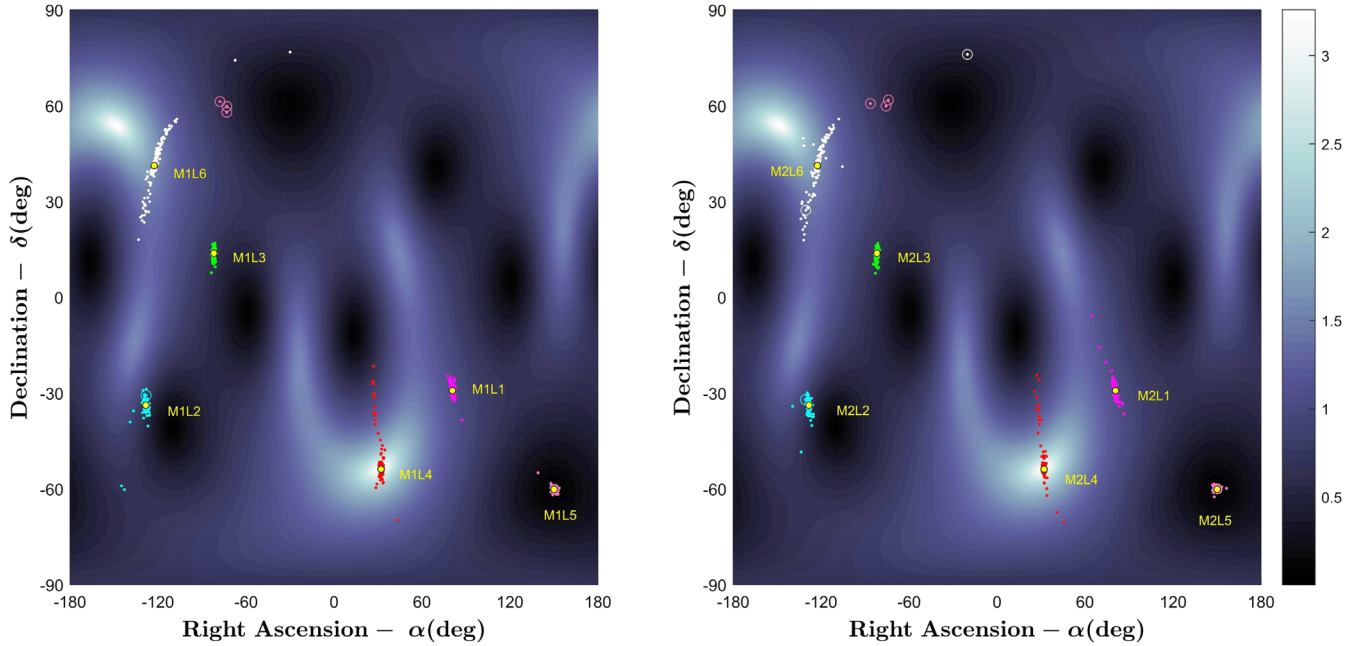


FIG. 4. Estimated sky locations for the mass sets M_1 ($m_1 = 1.4 M_\odot, m_2 = 1.4 M_\odot$) and M_2 ($m_1 = 4.6 M_\odot, m_2 = 1.4 M_\odot$). The true sky locations are indicated with yellow dots and listed in Table II. Estimated sky locations associated with a particular true location have the same color. Open circles with dots correspond to the data realizations where the coherent search statistic found by PSO failed to exceed the coherent fitness at the true signal parameter, $\rho < \Gamma(\theta_{\text{true}})$, even for $N_{\text{runs}} = 24$ independent PSO runs. The background gray-scale image in both panels is identical and shows the condition number sky map for the HLVK network corresponding to $\psi = \pi/6$.

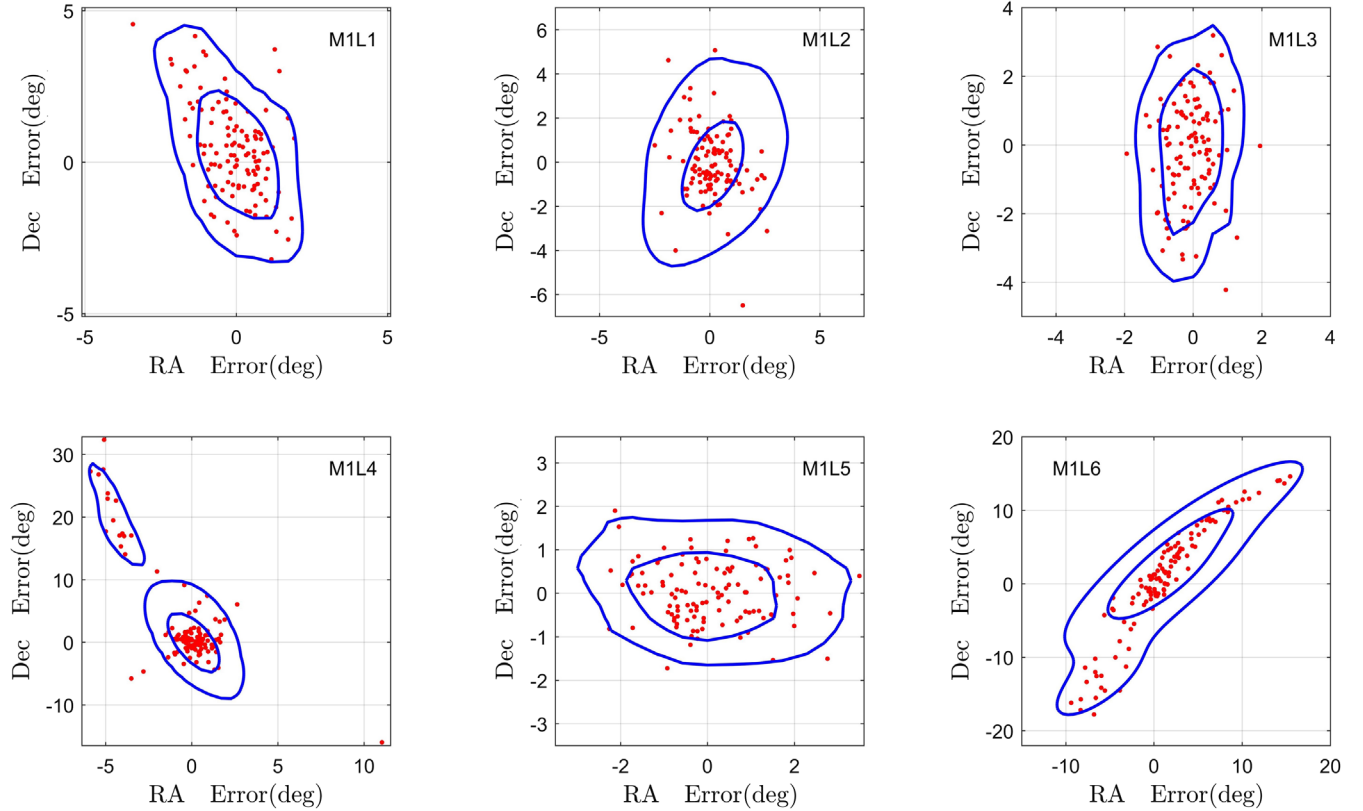


FIG. 5. Estimated sky locations (red dots) associated with the set M_1 ($m_1 = 1.4 M_\odot, m_2 = 1.4 M_\odot$) of sources. In each panel, the origin is centered at the true location of the source. The axes show the deviation of the estimated values of α and δ from their true values. Each panel also shows the contour levels of the bivariate probability density function, estimated using kernel density estimation (KDE) [48], that enclose 68% and 95% of the points. In these figures, the view has been zoomed in to show only the estimated locations that fall within or around the outer contour.

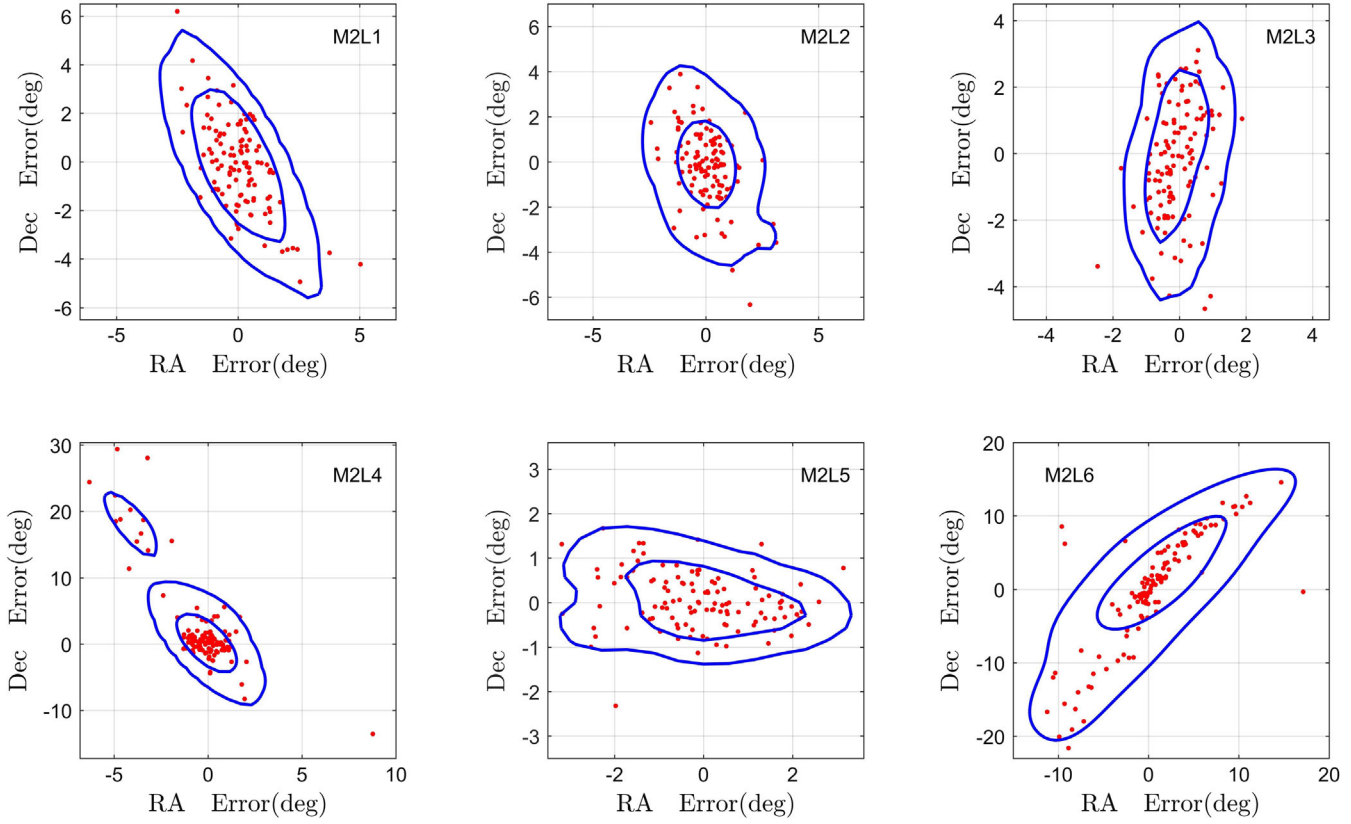


FIG. 6. Estimated sky locations (red dots) associated with the set M2 ($m_1 = 4.6 M_\odot, m_2 = 1.4 M_\odot$) of sources. In each panel, the origin is centered at the true location of the source. The axes show the deviation of the estimated values of α and δ from their true values. Each panel also shows the contour levels of the bivariate probability density function, estimated using kernel density estimation (KDE), [48] that enclose 68% and 95% of the points. In these figures, the view has been zoomed in to show only the estimated locations that fall within or around the outer contour.

assumed from Fisher-information-matrix-based analyses [50] that the correlation between the sky angles, α and δ , and chirp time parameters is negligible. While this result, which strictly holds only for asymptotically large SNRs, is

borne out by our simulation for the majority of cases, there are some sky locations for both the M1 and M2 sets where this does not hold. For example, for M1, there are two locations, L6 and L2, where the sample correlation

TABLE III. Sample mean and standard deviation (SD) of signal parameter estimates. The estimates of the binary component masses, m_1 and m_2 , are derived from those of the chirp time parameters τ_0 and $\tau_{1.5}$ using the relations given in the Appendix.

Source	τ_0 (seconds)		$\tau_{1.5}$ (seconds)		α (degrees)		δ (degrees)		$m_1 (M_\odot)$		$m_2 (M_\odot)$	
	Mean	SD	Mean	SD	Mean	SD	Mean	SD	Mean	SD	Mean	SD
M1L1	24.848	0.017	0.866	0.018	80.78	1.13	-28.90	1.79	1.491	0.138	1.299	0.089
M1L2	24.846	0.048	0.863	0.036	-128.61	2.57	-34.40	3.68	1.502	0.161	1.282	0.099
M1L3	24.848	0.023	0.863	0.022	-82.03	0.64	13.55	1.59	1.471	0.151	1.311	0.089
M1L4	24.849	0.024	0.866	0.025	31.73	2.09	-51.02	7.73	1.506	0.174	1.284	0.104
M1L5	24.849	0.018	0.866	0.018	150.09	1.56	-60.10	0.84	1.499	0.145	1.292	0.092
M1L6	24.849	0.022	0.865	0.023	-120.20	10.96	42.37	8.95	1.498	0.157	1.291	0.098
M2L1	9.750	0.023	0.728	0.025	80.61	2.25	-29.06	3.26	4.594	0.266	1.406	0.077
M2L2	9.747	0.023	0.725	0.022	-128.41	1.47	-34.17	2.09	4.559	0.247	1.415	0.080
M2L3	9.748	0.016	0.726	0.018	-82.02	0.65	13.52	1.79	4.570	0.189	1.410	0.052
M2L4	9.752	0.015	0.731	0.016	31.83	2.15	-51.74	6.92	4.623	0.164	1.396	0.042
M2L5	9.750	0.023	0.728	0.021	150.08	1.46	-60.11	0.63	4.590	0.239	1.407	0.088
M2L6	9.748	0.025	0.726	0.022	-122.14	5.27	41.26	7.85	4.563	0.272	1.415	0.103

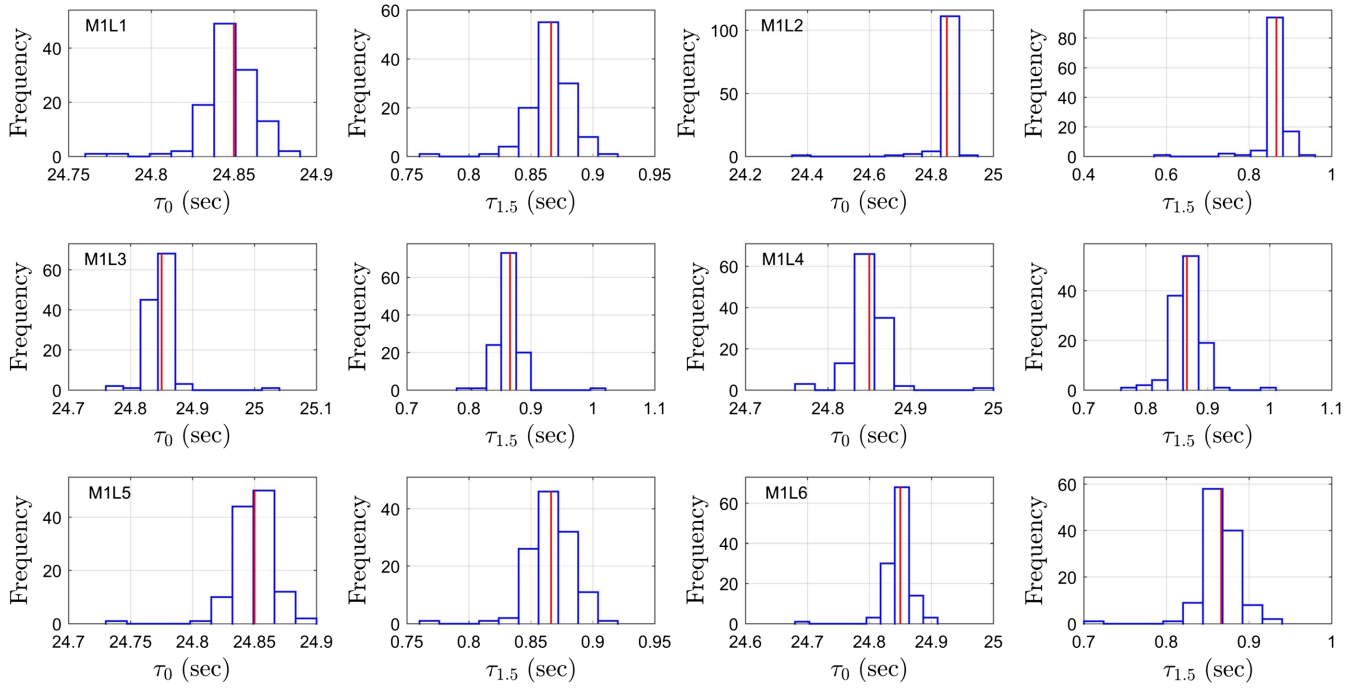


FIG. 7. Histograms of estimated chirp times, τ_0 and $\tau_{1.5}$, for all locations and mass set M1 ($1.4 M_\odot$ and $1.4 M_\odot$). The true values of the chirp times are shown by the red line in each plot. For each source sky location, the τ_0 and $\tau_{1.5}$ distributions are adjacent and on the same row, with the $\tau_{1.5}$ distribution always to the right of the τ_0 one.

coefficients are -0.452 and 0.416 , respectively, while it is low (absolute value $\lesssim 0.24$) elsewhere. Thus, the Fisher information may not be a good predictor of covariances between parameters for all source locations.

C. Computational cost

Obtaining the coherent fitness value for each PSO particle is the computationally most expensive step. The calculation of a single fitness value requires (i) the

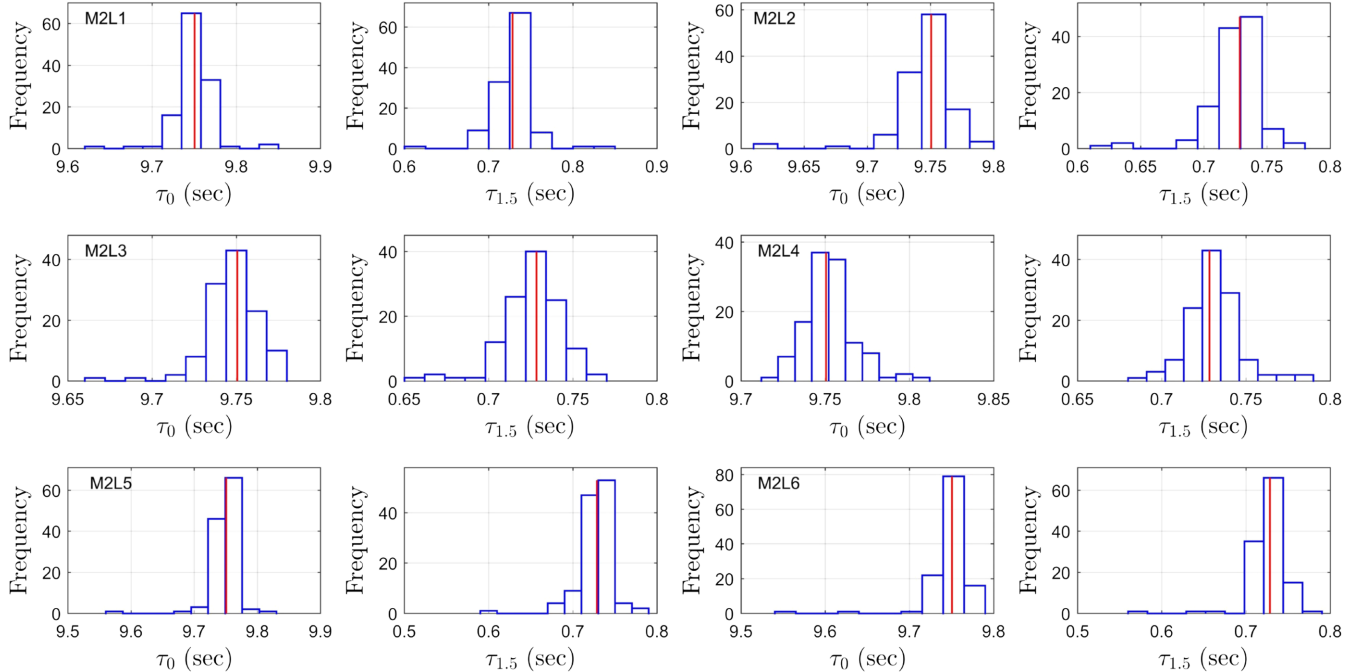


FIG. 8. Histograms of estimated chirp times, τ_0 and $\tau_{1.5}$, for all locations and mass set M2 ($4.6 M_\odot$ and $1.4 M_\odot$). The true values of the chirp times are shown by the red lines. For each source sky location, the τ_0 and $\tau_{1.5}$ distributions are adjacent and on the same row, with the $\tau_{1.5}$ distribution always to the right of the τ_0 one.

TABLE IV. Sample pairwise correlation coefficients of parameters. The parameter pairs are listed in the headings of the columns.

Source	$(\tau_0, \tau_{1.5})$	(α, δ)	(τ_0, α)	(τ_0, δ)	$(\tau_{1.5}, \alpha)$	$(\tau_{1.5}, \delta)$
M1L1	0.933	-0.618	0.152	-0.111	0.165	-0.096
M1L2	0.955	0.725	0.223	0.435	0.105	0.310
M1L3	0.959	0.174	-0.231	-0.179	-0.263	-0.163
M1L4	0.972	-0.791	-0.151	0.020	-0.144	0.051
M1L5	0.951	-0.426	-0.206	0.120	-0.229	0.150
M1L6	0.926	0.806	-0.452	-0.304	-0.345	-0.253
M2L1	0.970	-0.891	0.054	-0.025	0.045	-0.028
M2L2	0.947	-0.003	0.416	0.171	0.259	0.222
M2L3	0.935	0.305	-0.067	-0.034	-0.070	-0.011
M2L4	0.928	-0.794	0.011	0.081	0.058	0.031
M2L5	0.956	-0.147	0.093	-0.122	0.024	-0.095
M2L6	0.959	0.821	0.018	0.056	0.015	0.067

generation of two template waveforms [Eqs. (21)–(22)] in the Fourier domain, (ii) taking a sample-wise product of the data with each of the template waveforms [Eq. (24)], and (iii) taking the inverse FFT of each such product sequence [16]. The computational cost of each fitness evaluation in the PSO-based approach is identical to those of other stochastic optimization algorithms, such as MCMC, that have been used for fully coherent all-sky searches.

Among the above operations, the generation of template waveforms is the computationally most expensive step [51]. In situations where a grid-based search for the global maximum is computationally feasible, template waveforms can be precomputed and stored in advance, thus saving the cost of generating waveforms on the fly. Stochastic search algorithms do not use precomputed waveforms and, hence, must contend with this extra cost.

Several schemes [52–55] have been constructed to speed up waveform generation but we have not implemented any of these in our code so far. Besides this, our code is written entirely in Matlab and suffers a penalty in speed as a result. Thus, the wall-clock execution time of our code is not the correct metric to use for judging the computational savings brought about by PSO. The only useful metric for comparing PSO with other methods is the total number of fitness evaluations. Given the same code for evaluating the fitness function, algorithms that get by using a smaller number of evaluations will automatically have a better execution speed.

Since the termination criterion used for PSO in this paper is simply the number of iterations, there is an upper limit to the total number of fitness evaluations of 40 (number of particles) \times 500 (number of iterations) \times 12 (number of PSO runs) = 2.4×10^5 . However, the actual number of fitness evaluations is generally lower because of the boundary condition used, which allows particles to escape the search space. Particles outside the search space do not evaluate their fitness until they are

TABLE V. Statistical summary of the number of fitness evaluations for the two hypotheses under which data realizations were generated. The sample minimum, maximum, average, and standard deviation (SD) of the number of fitness evaluations are calculated over all the data realizations used for each hypothesis.

	Min	Max	Mean	SD
Signal absent (H_0)	163908	230808	210920	10758
Signal present (H_1)	193620	232716	221875	5373

pulled back in. Thus, the number of fitness evaluations can fluctuate across data realizations. Table V lists a statistical summary of the number of fitness evaluations obtained across all data realizations and all sources.

We see that the mean number of fitness evaluations is slightly lower in the case where a signal is absent. Thus, particles have an enhanced tendency to exit the search space boundary when a signal is absent. This may be a result of the fact that the contrast between the values at the local maxima of the fitness function is less pronounced in this case. Since most of the data from a GW detector consists of only noise, the fitness evaluation count for the signal absent case is more representative of the computational cost that will be incurred in practice.

VI. CONCLUSION

This paper presents a study of a PSO-based approach to solving the computational challenge, stemming from the necessity to carry out a high-dimensional numerical optimization task, in a fully coherent all-sky search for CBC signals.

At an astrophysically realistic signal strength (e.g., the SNR_{opt} used here matches $\text{SNR}_{\text{opt}} = 13$ for GW151226), we find that the best fitness value returned by PSO can approximate the GLRT quite effectively, suffering $\leq 2.5\%$ loss in detection probability, while using $< 1/10$ the number of likelihood evaluations needed for the grid-based or Bayesian searches. It is important to emphasize here that we are not altering the standard representation of CBC waveforms or approximating the likelihood function in any way. Any alternative scheme for likelihood or waveform calculation can be substituted without affecting the PSO algorithm itself.

A comparison of our parameter estimation results with theoretical bounds derived from a Fisher information analysis is not meaningful at the SNR value considered in this paper. This is because several studies have shown [56,57] that these bounds are reached only at significantly higher SNR_{opt} values.

A direct comparison with existing parameter estimation results from Bayesian approaches is difficult, since the definition of error in a Bayesian analysis differs from the frequentist one. Error in a Bayesian analysis is a measure of the spread of the posterior probability distribution.

The latter can be obtained even for a single data realization. The frequentist error is a measure of the spread of the point estimates over an ensemble of data realizations. Nonetheless, pending a future apples-to-apples comparison of Bayesian and frequentist errors on identical data realizations, we find that the best-case error of ~ 10 deg 2 in sky position from PSO is near the expected ballpark at the value of SNR_{opt} used here. For example, in [58] the sky location error for a signal with $\text{SNR}_{\text{opt}} = 29.6$, $m_1 = 1.5 M_{\odot}$, $m_2 = 2.0 M_{\odot}$, and the HLV network was found to be 3 deg 2 .

Although our results have been obtained for the ideal case of Gaussian, stationary noise, the computational cost will not change significantly for real detector noise. Recall that we are using PSO only for locating the global maximum of a fitness function. As long as the nature of this fitness function, in terms of the density of local peaks and the contrast in their values, does not change drastically, PSO will have the same performance. This is already evident when the computational cost of PSO is compared for the signal present and signal absent cases. We expect the change in the nature of the fitness function between these two cases to be far more significant than that between ideal and real detector noise.

A similar conclusion regarding computational cost will hold if different detector noise PSDs are used. In the case of inspiral signals, the global maximum lies along a ridge in parameter space and the first step towards success for PSO is to land somewhere on this ridge. Having different noise PSDs will not significantly affect the ruggedness of the fitness function, which comes from the presence of noise, but the ridge itself will become less sharply defined. The latter will happen because the maximum likelihood method automatically deemphasizes the contribution of a detector with higher noise, which can be viewed as an effective reduction in the number of detectors. This worsens parameter estimation errors, which is equivalent to broadening the likelihood function. Hence, it will become easier for PSO to locate the ridge feature at a similar or even lower computational cost.

We have run PSO on a rectangular search region consisting of independent upper and lower bounds on each parameter. This implies that the search range for each chirp time includes unphysical values. However, our results demonstrate that the probability of the global maximum straying into the unphysical region at the value of SNR_{opt} used is negligible. This need not be true when the data contain pure noise, and this may affect detection performance by increasing the false alarm probability somewhat. A rigorous study of this issue is postponed to future work.

Our results show that PSO offers a promising approach to realize a constantly on, fully coherent all-sky CBC search. Future investigations should address the following outstanding issues: (i) a determination of wall-clock time savings after incorporating state-of-the-art waveform

generation and likelihood evaluation techniques; (ii) reducing the instances of failure in locating the global maximum by trying out well-studied variants of PSO (for example, in [31], the neighborhood best, rather than global best, variant of PSO was found to perform significantly better); (iii) extension of the analysis to the computationally more demanding case of aLIGO noise power spectral density.

ACKNOWLEDGMENTS

We thank Y. Wang for sharing the kernel density estimation codes for sky localization studies. Most of the computation was done on “Thumper,” a computer cluster funded by National Science Foundation (NSF) MRI Grant No. CNS-1040430. T. S. W. acknowledges help from R. Jackson, manager of Thumper, in using the cluster. We thank M. Zanolin, E. Schlegel, J. Romano, and S. Mukherjee for helpful discussions. The contribution of S. D. M. to this paper was supported by NSF Grants No. PHY-1505861 and No. HRD-0734800.

APPENDIX: FUNCTIONAL FORMS OF PHASE PARAMETERS

Let M , μ , and η denote the total mass, the reduced mass, and the symmetric mass ratio of the compact binary system, respectively. Let f_* be the lower cutoff frequency of the detector. Then for $m_1 > m_2$, the chirp times are given by

$$\tau_0 = \frac{5}{256\pi} f_*^{-1} \left(\frac{GM}{c^3} \pi f_* \right)^{-5/3} \eta^{-1}, \quad (\text{A1})$$

$$\tau_1 = \frac{5}{192\pi} f_*^{-1} \left(\frac{GM}{c^3} \pi f_* \right)^{-1} \eta^{-1} \left(\frac{743}{336} + \frac{11}{4} \eta \right), \quad (\text{A2})$$

$$\tau_{1.5} = \frac{1}{8} f_*^{-1} \left(\frac{GM}{c^3} \pi f_* \right)^{-2/3} \eta^{-1}, \quad (\text{A3})$$

$$\begin{aligned} \tau_2 = & \frac{5}{128\pi} f_*^{-1} \left(\frac{GM}{c^3} \pi f_* \right)^{-1/3} \\ & \times \eta^{-1} \left(\frac{3058673}{1016064} + \frac{5429}{1008} \eta + \frac{617}{144} \eta^2 \right), \end{aligned} \quad (\text{A4})$$

where

$$M = (m_1 + m_2), \quad \mu = \frac{m_1 m_2}{M}, \quad \text{and} \quad \eta = \frac{\mu}{M}. \quad (\text{A5})$$

All four chirp time parameters are functions of m_1 and m_2 , implying that only two of them are independent. We chose τ_0 and $\tau_{1.5}$ as independent parameters to characterize the signal. Estimated values of τ_0 and $\tau_{1.5}$ were used to derive values for M and μ using the following equations:

$$\mu = \frac{1}{16f_*^2} \left(\frac{5}{4\pi^4 \tau_0 \tau_{1.5}^2} \right)^{1/3} \left(\frac{G}{c^3} \right)^{-1}, \quad (\text{A6})$$

$$M = \frac{5}{32f_*} \left(\frac{\tau_{1.5}}{\pi^2 \tau_0} \right) \left(\frac{G}{c^3} \right)^{-1}. \quad (\text{A7})$$

The parameters α_i , $i = 0, 1, \dots, 4$ in the phase function $\Psi(f)$ [Eq. (17)] are given by

$$\begin{aligned} \alpha_0 &= 2\pi f_* \frac{3\tau_0}{5}, & \alpha_1 &= 0, & \alpha_2 &= 2\pi f_* \tau_1, \\ \alpha_3 &= -2\pi f_* \frac{3\tau_{1.5}}{2}, & \alpha_4 &= 2\pi f_* 3\tau_2. \end{aligned} \quad (\text{A8})$$

-
- [1] B. P. Abbott *et al.* (LIGO Scientific Collaboration, Virgo Collaboration), *Phys. Rev. Lett.* **116**, 061102 (2016).
- [2] B. P. Abbott *et al.* (LIGO Scientific Collaboration, Virgo Collaboration), *Phys. Rev. Lett.* **116**, 241102 (2016).
- [3] B. P. Abbott *et al.* (LIGO Scientific Collaboration, Virgo Collaboration), *Phys. Rev. D* **93**, 122003 (2016).
- [4] B. P. Abbott *et al.* (LIGO Scientific Collaboration, Virgo Collaboration), *Phys. Rev. Lett.* **116**, 241103 (2016).
- [5] B. Abbott *et al.*, *Classical Quantum Gravity* **32**, 074001 (2015).
- [6] F. Acernese *et al.*, *Classical Quantum Gravity* **32**, 024001 (2015).
- [7] K. Somiya, *Classical Quantum Gravity* **29**, 124007 (2012).
- [8] C. S. Unnikrishnan, *Int. J. Mod. Phys. D* **22**, 1341010 (2013).
- [9] S. Fairhurst, *New J. Phys.* **13**, 069602 (2011).
- [10] B. P. Abbott *et al.* (LIGO Scientific Collaboration, Virgo Collaboration), *Astrophys. J.* **826**, L13 (2016).
- [11] B. S. Sathyaprakash and S. V. Dhurandhar, *Phys. Rev. D* **44**, 3819 (1991).
- [12] S. M. Kay, *Fundamentals of Statistical Signal Processing* (Prentice Hall, Englewood Cliffs, NJ, 1993), Vols. 1–2.
- [13] A. Pai, S. Dhurandhar, and S. Bose, *Phys. Rev. D* **64**, 042004 (2001).
- [14] B. J. Owen and B. S. Sathyaprakash, *Phys. Rev. D* **60**, 022002 (1999).
- [15] I. W. Harry and S. Fairhurst, *Phys. Rev. D* **83**, 084002 (2011).
- [16] S. Bose, T. Dayanga, S. Ghosh, and D. Talukder, *Classical Quantum Gravity* **28**, 134009 (2011).
- [17] R. Lynch, S. Vitale, R. Essick, E. Katsavounidis, and F. Robinet, [arXiv:1511.05955v2](https://arxiv.org/abs/1511.05955v2).
- [18] D. Macleod, I. W. Harry, and S. Fairhurst, *Phys. Rev. D* **93**, 064004 (2016).
- [19] W. R. Gilks, S. Richardson, and D. J. Spiegelhalter, *Markov Chain Monte Carlo in Practice* (Chapman and Hall/CRC Press, London, 1996).
- [20] M. van der Sluys, V. Raymond, I. Mandel, C. Rver, N. Christensen, V. Kalogera, R. Meyer, and A. Vecchio, *Classical Quantum Gravity* **25**, 184011 (2008).
- [21] L. P. Singer and L. R. Price, *Phys. Rev. D* **93**, 024013 (2016).
- [22] N. J. Cornish, [arXiv:1606.00953](https://arxiv.org/abs/1606.00953).
- [23] C. Pankow, P. Brady, E. Ochsner, and R. O’Shaughnessy, *Phys. Rev. D* **92**, 023002 (2015).
- [24] K. Cannon, A. Chapman, C. Hanna, D. Keppel, A. C. Searle, and A. J. Weinstein, *Phys. Rev. D* **82**, 044025 (2010).
- [25] S. E. Field, C. R. Galley, F. Herrmann, J. S. Hesthaven, E. Ochsner, and M. Tiglio, *Phys. Rev. Lett.* **106**, 221102 (2011).
- [26] J. Kennedy and R. C. Eberhart, Particle swarm optimization, in *Proceedings International Conference on Neural Networks* (IEEE, Perth, 1995), pp. 1942–1948.
- [27] Y. Shi, Particle swarm optimization: developments, applications and resources, in *Proceedings Evolutionary Computation* (IEEE, Seoul, 2001).
- [28] J. Prasad and T. Souradeep, *Phys. Rev. D* **85**, 123008 (2012).
- [29] A. Rogers and J. D. Fiege, *Astrophys. J.* **727**, 80 (2011).
- [30] Y. Wang and S. D. Mohanty, *Phys. Rev. D* **81**, 063002 (2010).
- [31] Y. Wang, S. D. Mohanty, and F. A. Jenet, *Astrophys. J.* **795**, 96 (2014).
- [32] Y. Bouffanais and E. K. Porter, *Phys. Rev. D* **93**, 064020 (2016).
- [33] A. Lazzarini and R. Weiss, LIGO Technical Document, Report No. LIGO-E950018, <https://dcc.ligo.org/LIGO-E950018/public>.
- [34] A. Leick, *GPS Satellite Surveying* (Wiley, New York, 2004).
- [35] P. Jaranowski, K. D. Kokkotas, A. Krolak, and G. Tsegas, *Classical Quantum Gravity* **13**, 1279 (1996).
- [36] S. Klimenko, S. Mohanty, M. Rakhmanov, and G. Mitselmakher, *Phys. Rev. D* **72**, 122002 (2005).
- [37] S. D. Mohanty, M. Rakhmanov, S. Klimenko, and G. Mitselmakher, *Classical Quantum Gravity* **23**, 4799 (2006).
- [38] M. Rakhmanov, *Classical Quantum Gravity* **23**, S673 (2006).
- [39] B. Althouse, S. Hand, L. Jones, A. Lazzarini, and R. Weiss, LIGO Technical Document, Report No. LIGO-P000006, <https://dcc.ligo.org/P000006/public>.
- [40] <http://www.ligo.org/scientists/GW100916/detectors.txt>.
- [41] L. Blanchet, T. Damour, B. R. Iyer, C. M. Will, and A. G. Wiseman, *Phys. Rev. Lett.* **74**, 3515 (1995).
- [42] W. Helstrom, *Elements of Signal Detection and Estimation* (Prentice Hall, Englewood Cliffs, NJ, 1995).
- [43] F. Solis and R. Wets, *Math. Oper. Res.* **6**, 19 (1981).
- [44] D. Bratton and J. Kennedy, Defining a standard for particle swarm optimization, in *Proceedings Swarm Intelligence Symposium* (IEEE, Honolulu, 2007).

- [45] R. Poli, J. Kennedy, and T. Blackwell, *Swarm Intell.* **1**, 33 (2007).
- [46] A. P. Engelbrecht, *Fundamentals of Computational Swarm Intelligence* (Wiley, New York, 2005).
- [47] J. Kennedy and R. Mendes, in *IEEE Transactions on Systems, Man, and Cybernetics, Part C (Applications and Reviews)* (IEEE, 2006), Vol. 36, pp. 515–519.
- [48] V. A. Epanechnikov, *Theory Probab. Appl.* **14**, 153–158 (1967).
- [49] B. S. Sathyaprakash, *Phys. Rev. D* **50**, R7111 (1994).
- [50] L. P. Singer and L. R. Price, *Phys. Rev. D* **93**, 024013 (2016).
- [51] A. Buonanno, B. R. Iyer, E. Ochsner, Y. Pan, and B. S. Sathyaprakash, *Phys. Rev. D* **80**, 084043 (2009).
- [52] R. J. E. Smith, K. Cannon, C. Hanna, D. Keppel, and I. Mandel, *Phys. Rev. D* **87**, 122002 (2013).
- [53] S. E. Field, C. R. Galley, J. S. Hesthaven, J. Kaye, and M. Tiglio, *Phys. Rev. X* **4**, 031006 (2014).
- [54] M. Pürer, *Classical Quantum Gravity* **31**, 195010 (2014).
- [55] J. Blackman, S. E. Field, C. R. Galley, B. Szilagyi, M. A. Scheel, M. Tiglio, and D. A. Hemberger, *Phys. Rev. Lett.* **115**, 121102 (2015).
- [56] R. Balasubramanian, B. S. Sathyaprakash, and S. V. Dhurandhar, *Phys. Rev. D* **53**, 3033 (1996).
- [57] M. Vallisneri, *Phys. Rev. D* **77**, 042001 (2008).
- [58] C. Rover, R. Meyer, and N. Christensen, *Phys. Rev. D* **75**, 062004 (2007).